IIT, Madras

Morphological characterisation of 2D packing with bi-disperse particles

Mingrui Dong[1] · **Joerg Reimann**[2] · **Ratna Kumar Annabattula**[3] · **Yixiang Gan**[1,4]

Abstract The morphological structure of granular materials can dominate their mechanical, hydraulic, electrical, and thermal properties; thus, the formation of order and disorder arrangement of particles is the key characteristic to describe such micro-structures. During the packing procedure, external energy input and perturbations, such as dynamic cyclic load, and the particle size distribution were mentioned by many previous works to be significant in controlling the structure. This study explores order to disorder transition within 2D binary granular assemblies under vibration. A numerical packing method combining particle size growth and dynamic vibration is implemented and verified against experiments to achieve desired packing structure. The Bond orientation order number and pair distribution function are used as indices for characterising the morphological structure. Our packing simulation results show a combination of appropriate vibration and a proper particle size growth rate can facilitate the formation of granular crystallisation. Additionally, for binary packing, the size ratio, and the number fraction of small particles can play a critical role in determining the morphological transformation.

✉ Yixiang Gan
  yixiang.gan@sydney.edu.au

1 School of Civil Engineering, The University of Sydney, Sydney, NSW 2006, Australia

2 Karlsruhe Institute of Technology, P.O. Box 3640, 76021 Karlsruhe, Germany

3 Department of Mechanical Engineering, Indian Institute of Technology Madras, Chennai 600036, India

4 The University of Sydney Nano Institute, The University of Sydney, Sydney, NSW 2006, Australia

1 Introduction

The morphological structure of granular materials is dominant for the overall effective properties, such as mechanical response to external load [1–3], hydraulic permeability and cohesion [4, 5], thermal conductivity [6, 7] and electrical conductivity [8–11]. The order and disorder arrangement of particles can be used to characterise the packing structure of overall assemblies. The studies on packing structure of granular materials range from observing jamming conditions [12–14], reaching random close packing limits [15–19] and generating granular crystallisation structures through different wall conditions [15, 20–22]. The earlier work mainly utilised the mono-sized spherical particles as the simplest granular systems. An obvious question here is how to control the resulting packing structure by mixing different sizes.

Recent studies have been focusing on characterising the structure through packing fraction. In 2D conditions, mono-disperse samples have a typical packing fraction $\phi \approx 0.84$ for random close packing [23], and with a much lower value $\phi \approx 0.64$ in 3D condition [13, 23–26]. Whilst bi-disperse particles typically raise the resulting ϕ in 2D [15, 25], further polydispersity can raise ϕ to closely 1 when pore space between large particles can be fulfilled hierarchically with smaller ones in the Apollonian setting [27]. Due to the wall effect, the structure near the wall is more likely to show ordered arrangement compared with the bulk region [20, 21]. To further characterise the overall morphological structure, the pair distribution function, $g(r)$, can be used. The $g(r)$ function performs as a long-range

🅰 Springer

fluctuation with high amplitude when structure is ordered and short-ranged fluctuation with a low amplitude when structure is disordered [28–30]. Bond orientation order number,ψ, has been applied to quantitatively characterise the order state with a percentage of crystallised particles (grains), the grain size and grain orientation.

In granular materials, the particle size may not always be constant and individual particles may experience expansion or shrinkage under certain conditions, such as heating or cooling [7, 31], wetting or drainage [32–34]. The morphological structure can be crucially rearranged during those processes mentioned above. External dynamic loading also plays an important role. For example, granular samples can experience raised inter-particle force during a jammed condition under external dynamic loads [12]. A continuing increased load may gradually lead samples to elastic region, yielding and failure until the ultimate steady state is reached [35–37]. The granular skeleton evolvement during these processes have been studied both numerically [20, 38] and experimentally [12, 21]. When it is not jammed, the dynamic vibration with certain intensity can rearrange particles to a more ordered state with relatively low potential [39].

In this study, to control the degree of order and disorder in pseudo-2D granular assemblies, a combined procedure of particle size growth and dynamic vibration is applied to both mono-disperse and bi-disperse granular assemblies. Simulations are established using discrete element method (DEM) on the open-source platform LIGGGHTS. Firstly, the effectiveness of size growth rate and dynamic vibration is tested. By comparing the simulation with experiments, the method is verified through observing the degree of crystallisation and structure patterns. Secondly, the wall effect is examined to eliminate the finite size effect. Finally, the morphological structure evolution of bi-disperse cases is studied by varying the size ratio (η) and the number fraction of small particles (C_s).

2 Method

2.1 Discrete element method

The discrete element method (DEM) is adopted as the computational technique, which was firstly proposed by Cundall and Strack [40], and further improved by Walton [41] and Luding [42]. To simulate dynamic responses of granular assemblies, the model is established on the open-source platform LIGGGHTS [43]. The dynamic motion of particles and contact relation are governed by Newton's second law given by:

$$\begin{cases} F_n = k_n\delta_n - \beta_n v_n \\ F_t = k_t\delta_t - \beta_t v_t \end{cases} \tag{1}$$

where F is the contact force, k is the contact stiffness, δ is the overlap distance between the pair of particles in contact, β is the damping ratio, and v is the relative velocity of a contact pair, subscripts n and t represent normal and tangential effect, respectively. The frictional force, F_t, adopts the Coulomb friction criteria that $|F_t| \leq \mu|F_n|$, where μ is the friction coefficient. Since friction impedes and slows down the transition from disorder to order under the dynamic load [20], the frictionless cases are considered here to have a relatively fast simulation to reach the final stages. The parameters used in this study are listed in Table 1.

2.2 Simulation conditions

The modelling process is described below. A group of non-contact particles are created with random positions in a 2D square container domain, and the initial particle size is controlled such that $\phi_{\text{initial}} < 0.5$. The particle assembly is then settled under the gravitational acceleration, $g = 9.81$ m/s^2, as shown in Fig. 1a. After the kinetic energy, E_{kinetic}, is dissipated and is much smaller than the potential energy, e.g. $E_{\text{kinetic}} < E_{\text{potential}} \times 10^{-10}$ [42], the overall structure can be considered as a "steady state", and the hydraulic pressure remains constant. Particles then gradually grow to fill up the whole container, with a size growth rate setting as $\dot{\gamma} = \Delta d/d = 0.01$/s determined by a series of parametric studies which will be further discussed in Sect. 3. To make sure the contact duration in the dynamic process to be physically meaningful and steady for simulation, the parameters are controlled by checking the time scale $T_c = \sqrt{m/Ed_s} \gg \dot{\gamma}^{-1}$ [44], where m is the single particle mass, E is the young's modulus. Here, the time step is selected as 5×10^{-7} s. To minimise the unnecessary artificial viscosity, the coefficient of restitution is selected as 0.6 [20, 42].

A sinusoidal format vibration is applied to initiate and accelerate the transition of overall morphology from disorder to order (i.e. crystallisation) [20]. The direction of vibration is set to perpendicular to that of gravitational acceleration, g, illustrated in Fig. 1b. The horizontal shaking is controlled by the vibration intensity, $\Gamma = A(2\pi f)^2/g$, where A is the vibration amplitude, f is the frequency, g is the gravitational acceleration. The magnitude for Γ is controlled by varying the amplitude, and its effects will be further discussed in Sect. 3. The square container size is set to be consistent with that of the experiment 100 mm (Fig. 1b). To be noted, the vibration and size growth are adopted simultaneously (Fig. 1). A

Table 1 Parameters for simulations

Parameter	Value
Young's modulus, E (GPa)	110
Poisson ratio, v (–)	0.2
Mass density of particles, ρ_p (kg/m^3)	4750
Friction coefficient, μ (–)	0
Coefficient restitution (–)	0.6
Diameter of sphere, d (mono-disperse), d_s and d_l (bi-disperse) (mm)	4, 2.32, 1.6 (mono-disperse), d_s and d_l are controlled through η (bi-disperse)
Size ratio, η (–)	d_l/d_s = 1.03, 1.06, 1.1, 1.2, 1.3
Total particle number, N_t (–)	5000
Small particle number, N_s (–)	500, 1500, 2500, 3000, 3500, 4000, 4500
Number fraction of small particles, C_s (–)	N_s/N_t = 0.1, 0.3, 0.5, 0.6, 0.7, 0.8, 0.9
Container height/width (mm)	100/100
Gravitational acceleration, g (m/s^2)	9.81
Time step (s)	5×10^{-7}

target mean stress, σ_{mean}, is then set to stop the vibration and size growth. The target σ_{mean} is determined by the comparable simulation the same as experiments. A period of relaxation is set for the system to reach the steady state. It is also checked that the drop of the σ_{mean} is not larger than 4%.

Two main structural indices are adopted in this study to distinguish the order and disorder structure, and quantitatively describe the structure transition when varying binary mixture via η and C_s. Firstly, the pair distribution function, $g(r)$, reveals the probability density of particles that can be found in the shell area at a certain distance from the target particle. Through $g(r)$, a long-range fluctuation with relatively large amplitude (representing order structure) or a short-range fluctuation with relatively smaller amplitude

(representing disorder structure) can be used to characterise the particle arrangement. The adopted $g(r)$ can be shown in the function below [45]:

$$g(r) = \frac{1}{2\pi r(\Delta r)\rho_q(N_t - 1)} \sum_{j\neq k} \delta(r - |\overrightarrow{r}_{jk}|), \qquad (2)$$

where r is the distance between the centre of target particle and the midline of the shell, Δr is the shell thickness, ρ_q is the particle number density of the whole system, N_t is the total particle number, the summation of Dirac Delta function $\delta(r - |\overrightarrow{r}_{jk}|)$ indicate a scanning of all particles except target particles j and extract those located within the shell area. When applying $g(r)$, the Δr is chosen to be smaller than d_m, where $d_m = (d_s N_s + d_l N_l)/N_t$, which can facilitate the capture of sharp fluctuation. Here, Δr is set to be $0.1 \times d_m$. We represent the pair distribution function, $g(r)$, by normalising r with d_m.

To further quantitatively characterising the extent of order and disorder, the bond orientation number [20, 46], ψ, is used and showed by equation below:

$$\psi = \left| \frac{1}{N_{j,k}} \sum_{k=0}^{6} e^{6i\theta_{jk}} \right|, \qquad (3)$$

where $N_{j,k}$ is the neighbour number of target particle j, the summation traverses over the nearest neighbours with a cut-off distance calculated by radii of particles, as $R_j + R_k + 0.1 \times \min(R_k, R_j)$, θ_{jk} is the angle between the position vector of particles j and k and the coordination system is shown in Fig. 2a. A perfect hexagonal structure gives $\psi = 1$, and ψ approaches to 0 towards the extreme case of structural disorder. The threshold of ψ for crystallisation in this study is set to be $\psi \geq 0.75$ [20, 46]. The crystallised clusters (grains) can be further characterised by the grain orientation angle α as in Fig. 2b.

Fig. 1 Packing simulation: **a** A 2D granular assembly is created within the container domain ($D \times D$). The smaller particles are coloured in red, and the larger particles in grey. The inseted sketch in (**a**) containing two circles and springs illustrate the basic contact laws based on Hertzian contact. **b** Visualisation of a final packing structure extracted from one bi-disperse case. The arrows at the bottom illustrate the direction of vibration
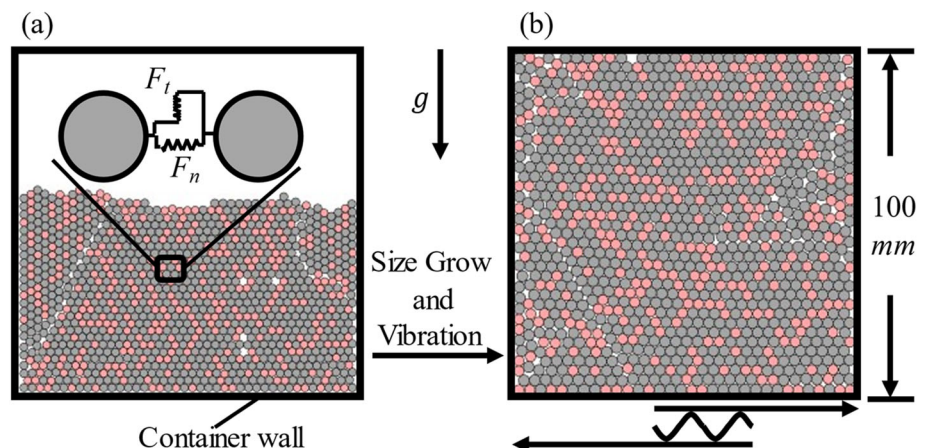
2.3 Confinement stress

The confinement stress state in 2D is obtained through the function [38]:

$$\sigma = \frac{1}{2V} \sum_{i \neq j} F_n \delta_{ij}, \tag{4}$$

where the V is the volume of the container, F_n is the normal force of each contact, δ_{ij} is the centre-to-centre distance of contact particle i and j. Since the above stress term is used for calculating the pressure inside the assembly, the tangential component does not contribute to this formular, see [38]. Moreover, the friction coefficient in these cases studied here is set to zero.

3 Packing simulation and validation

3.1 2D packing experiments

The 2D packing experiments are established using a square prismatic container with aluminium spheres with the aim to finally obtain a single layer of spheres with maximum coverage. The container is slightly inclined to the horizontal plane with the bottom edge, Fig. 4a, b being at the lowest position. Initially, locally, several layers of spheres are placed in the container. The container then is gently shaken (knocked) to ease the movement of particles and to obtain the maximum coverage. Individual spheres are filled in by hand in empty spaces to ensure that all voids with sufficiently large spaces are occupied. Experimental photos are taken at the end to capture the packing patterns of the

Fig. 2 The bond orientation order number ψ: **a** The angle of each position vector $\vec{jk}$ when taking the positive x-axis as the reference. **b** The crystallised grain (i.e. hexagonal structure) orientation angle, α, of each particle that is evaluated. Since the hexagonal structure is symmetric, the angle ranges from $0°$ to $60°$

single layer which are showed in Fig. 4a, b. The η for the bi-disperse sample in the experiment is 1.06 (Fig. 4b).

The objective here is to develop a simulation method to obtain desired packing structures comparable with experiments. The experimental setup is slightly different from the simulation described in Sect. 2.2, in terms of the "fill-in" and "knocking" processes. The experimental procedure involves a sequential fill-in process of particles, modelling of which can be computationally expensive. In simulations, the randomly pre-generated particle experiencing size growth can simplify and eliminate this time-consuming process, whilst keeping the results representative. The vibration is an effective method to accelerate simulations of crystallisation [16, 20], though the amplitude of vibration should be chosen carefully to introduce adequate perturbations to the system. Such a process is more efficient as compared to "knocking", since "knocking" with large time intervals is time-consuming and unnecessary in simulation.

3.2 Validation of packing simulation

To quantitatively compare the simulation and experimental results, the percentage of crystallised particles (PCP), i.e. evaluated with $\psi \geq 0.75$, is adopted as the criteria. The size growth rate, $\dot{\gamma}$, and vibration intensity, Γ, are studied parametrically. Here, the mono-disperse case, $d = 4$ mm and $N_t = 700$ are selected as the benchmark to verify the effectiveness of $\dot{\gamma}$ and Γ. To be consistent with the experiment, the external loadings are terminated after the particle diameter reached 4 mm, followed by a period of relaxation time. Note here the mean stress is not controlled but considered as an output of the simulation.

As can be observed in Fig. 3a, the optimum point for Γ locates at 2.0 where the PCP not only matches with the experiment but also the standard deviations of samples are minimised. The reasons can be explained that the smaller $\Gamma \approx 0.4$ is not effective to provide enough perturbation energy input, which hinders the rearrangement of particles into a low potential state. Conversely, the larger $\Gamma = 4$ and 8 can offer too much energy to keep the ordered arrangement to be stable which is manifested as the larger error.

Regarding the size growth rate, $\dot{\gamma}$, depicted in Fig. 3b, the $\dot{\gamma}$ at 2×10^{-9} leads the simulated PCP to be consistent with that of the experiment. The larger $\dot{\gamma} \geq 2 \times 10^{-8}$ is not able to provide enough time for the movement of particles during the disorder to order transition. The corresponding normalised stress, σ_{mean}/E, at each $\dot{\gamma}$ is showed by the secondary y axis on the right side of Fig. 3(b). It can be found that the higher the PCP is, the smaller stress is. Since PCP indicates the probability density of crystallised particles within the sample, the solid structure with higher PCP
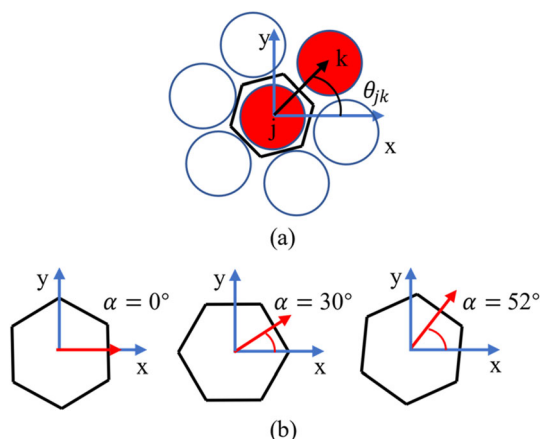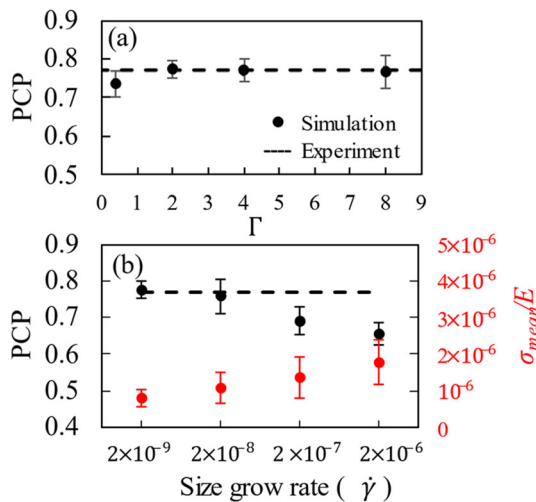
Fig. 3 Mono-disperse packing: **a** The PCP versus vibration intensity Γ. **b** The PCP versus Size growth rate $\dot{\gamma}$. In both (**a**) and (**b**), each point with errorbar indicates average results from 10 simulations

Fig. 4 **a**, **b** are experiments photos where (**a**) shows a mono-disperse case with sphere size, $d \approx 4$ mm, and **b** is a bi-disperse case with $d_s \approx 3$ mm and $d_l \approx 3.2$ mm. **c**, **d** are simulation results with the identical dimensional parameters as the experiments. The red boxes highlight the disordered clusters and dislocations within the sample

can occupy less space of the container with more compacted arrangements. Thus, the overall σ_{mean} can be minimised, and the normalised stress is inversely related to the PCP.

The normalised stress, σ_{mean}/E is monotonically related to the size growth rate and has the opposite trend compared to PCP. For the mono-disperse case, the optimum combination of size growth rate $\dot{\gamma} = 2 \times 10^{-9}$ and vibration intensity $\Gamma = 2$ can lead to the target PCP comparable with experiments, as shown in Fig. 3.

The simulation results exhibit quite similar patterns when comparing with the experiments, as shown in Fig. 4. The mono-disperse cases, Fig. 4a, c, both exhibit composition of hexagonal positioned particles with several disordered parts (marked by red boxes). The bi-disperse cases, Fig. 4b, d, both exhibit dislocation boundaries, which mostly originate from the wall region. All four cases show zigzag pattern at the left and right boundary at the wall. This may be caused by the direction of the gravitational acceleration, g, which is vertically downwards in the simulation. This structural arrangement may be more stable under gravity along this direction. Although g is mostly out of the plane in the experiments, there is a small g component pointing the direction similar with the simulation can appear.

3.3 Wall effects

To illustrate the wall effects, a series of simulations with different particle number, N_t, of mono-disperse particles are conducted. While keeping the container size constant, the ratio between container size and particle diameter, D/d,
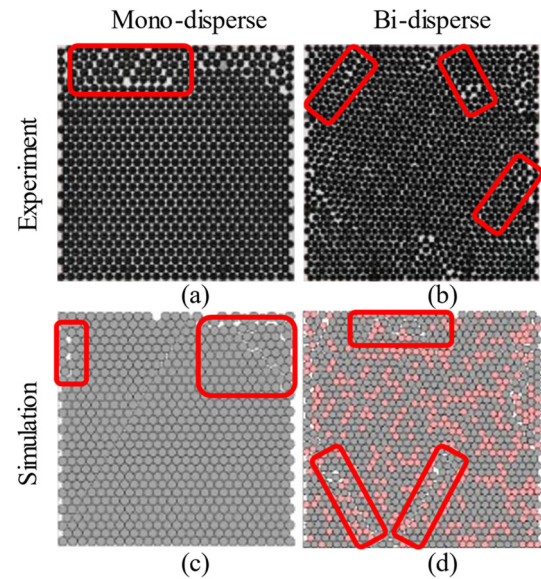
is varied during the test. As shown in Fig. 5, PCP increases sharply before $D/d \approx 70$ followed by a steady slow climb. The particle at the zigzag boundary of crystallised grains contact with the wall is not considered to belong to the grains. They are mostly located near the wall region (explained through Fig. 4) due to the effect of downward g, and normally it can be only one layer of particles. Besides, the wall effect was proved to be dominant in a granular system when a small distance, compared to the particle size, between walls exists [20, 21, 47]. Thus, the investigation of bi-disperse cases is then conducted using the $D/d \approx 70$ with $N_t = 5000$ particles in the 100 mm $\times$ 100 mm container.

4 Order and disorder structure in bi-disperse assemblies

The characterisation of morphological structure within the bi-disperse granular assemblies will be analysed by $g(r)$ and ψ. The size ratio, $\eta = d_l/d_s$, varies from 1.03 to 1.3 and small particle number fraction, $C_s = N_s/N_t$, ranges from 0.1 to 0.9.

In Fig. 6, four groups $g(r)$ fluctuate with the ascending r/d_m. The gradient grey scales (from light to dark) indicate the specific number fraction of small particles (C_s) rising from 0.1 to 0.9. The trend of the fluctuation shifts from long range with a large amplitude for $\eta = 1.06$, to short-
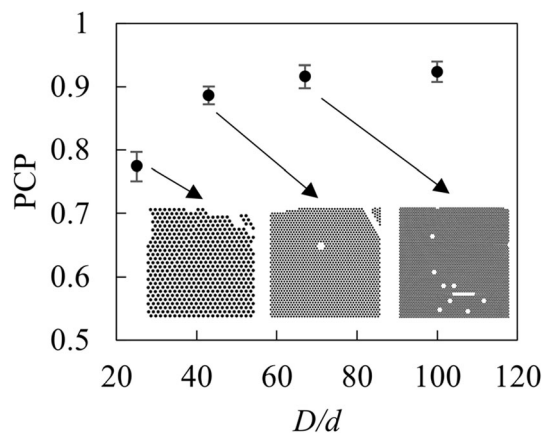
Fig. 5 Wall effects at varying ratios between container size, D, and particle size, d. The PCP shows an asymptote when D/d over 70, which indicates the wall effects are minimised. Three packing insets illustrate the packing structure of different D/d, showing only the crystallised particles

range with a small amplitude for $\eta = 1.3$. The mono-size case with the optimum ordered condition, e.g. PCP ≈ 0.91, is plotted using a red line as a reference to compare against all binary cases. The structure pattern of this reference line can be referred to Fig. 5, and $D/d \approx 70$. Thus, the smaller size contrast, $\eta = 1.06$ represents a more ordered structure, because a certain number of particles are more likely to be found at the specific distance from a target particle. In comparison, the larger size contrast, $\eta = 1.3$, exemplifies disordered structures. The probability density, $g(r)$, is small, which depicts low amplitude and short-range fluctuation. The high $C_s = 0.9$ and low $C_s = 0.1$ both have less noticeable effects on disturbing the ordered structure. The C_s in the range from 0.5 to 0.7 shows a clear transition to disorder structures, and under these conditions, the relatively smoother curve can be found in each η group. To clarify, since the $g(r)$ is observed regarding the mean diameter d_m, the first peak can be found to deviate from $r/d_m = 1$. The increase in C_s lead to the smaller fluctuation representing order to disorder transition. A bounce back with larger fluctuation when C_s further increases to 0.9 can be observed.

Crystallisation is a type of typical order structure with the hexagonal arrangement in 2D condition. The crystallisation within a mono-sized sphere assembly can be formed and observed when the granular sample is subjected to external loadings such as vibration [20, 22, 29], shear [48, 49] and compression [50]. Here, the morphological structure with order and disorder particle arrangements can be characterised by the PCP variation and crystallised grain orientation (Fig. 2). In Fig. 7, for $\eta = 1.06$, the PCP firstly decreases when C_s arise from 0.1 until reaching the minimum at roughly 0.5, then followed by a gradually rise. The PCP value at the bottom of each valley

slightly shifts corresponding to the C_s. The PCP for $\eta = 1.06$ and $\eta = 1.1$ reach the minimum when $C_s \approx 0.5$, whilst the cases $\eta = 1.2$ and $\eta = 1.3$ reach the minimum roughly at 0.7. This shift is consistent with several previous works reflected in the packing fraction [25, 51].

In Fig. 8, crystallised grains formed by ordered particles are depicted through a heat map. The inserted crystallised grain orientation plots show grain orientation angles from $0°$ to $60°$. It can be observed that mono-sized or nearly mono-sized case are highly likely to form a single crystalline grain, such cases can be found in Fig. 4a, c and Fig. 8 when $\eta = 1.06$, $C_s = 0.9$. On the contrary, the bi-disperse case tends to form disordered or polycrystalline grains, such cases can be found in Fig. 4b, d and Fig. 8 when $\eta = 1.2$, $C_s = 0.9$. As portrayed in the crystallised grain orientation plots in Fig. 8, when varying the combination of η and C_s, it is apparent that the morphological structure also differs. When the size ratio is raised to 1.06, independent of number fraction, C_s, the packing starting to transfer from order to disorder and polycrystalline structure start to form. Either raising C_s from 0.1 or decreasing C_s from 0.9 can further suppress the formation of polycrystalline towards large-size grains, taking $\eta = 1.3$, $C_s = 0.9$ and $\eta = 1.3$, $C_s = 0.7$ as examples. The later exhibits only sparse small grains. The rising η can subdivide initially connected grains into several small parts with diverse grain angles. This phenomenon can be the evidence of the fluctuation for $g(r)$ in Fig. 6.

Regarding the polycrystalline grain structure, the orientation of each grain can be different from each other. Depicted by grain orientation plots in Fig. 8, both η and C_s can be crucial to the diversity of resulting grain orientation. This diversity of grain orientation angles is portrayed by the degree of colourfulness, e.g. a polycrystalline case with a diversity of grain angle can be found when $\eta = 1.2$ and $C_s = 0.7$, while an almost single-crystalline case is showed when $\eta = 1.06$ and $C_s = 0.9$ (Fig. 8).

Since σ_{mean} is kept constant for each case, e.g. at the end of the relaxation stage, the structure evolution can also be characterised by the variation of packing fraction ϕ and the mean diameter d_m. In Fig. 9a, the d_m of particles is linearly related to the packing fraction. The more even the particles sizes are, the larger d_m is needed to form the packing with the specific σ_{mean}. PCP can also be seen as linearly related to ϕ before reaching 0.87, and followed by an almost constant trend showed in Fig. 9b. This result is consistent with that of the 2D setup using circular discs mentioned by Donev, Torquato [23].

To be clarified, it should be noted that there are limitations when comparing the simulation with experiments in this study. For bi-disperse samples in 2D simulations here, centres of all particles are always in one plane, whilst it is not the case in the experiments. In experiments, described
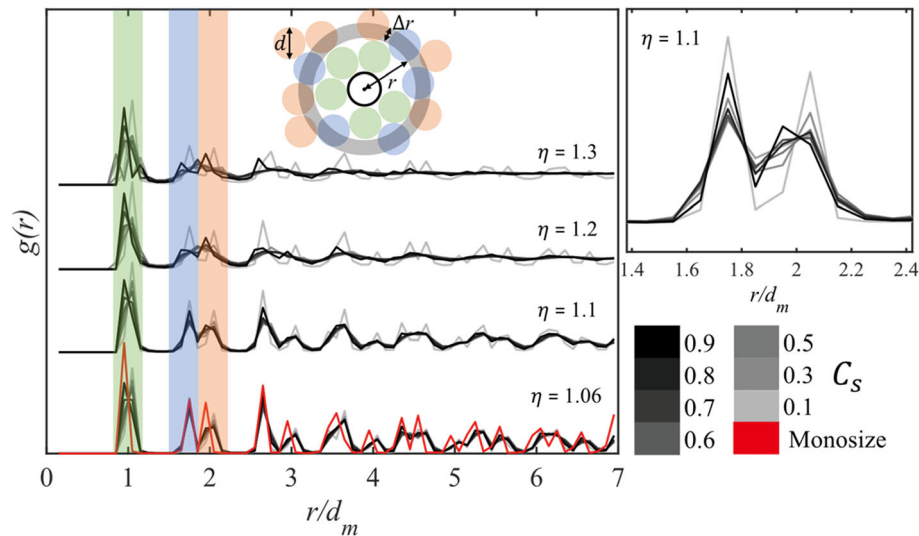
Fig. 6 Radial distribution function $g(r)$ with varying η and C_s. The red line represents the mono-size case which can be a reference compared with the bi-disperse cases. Blue particles (with diameter d) can be identified that they all located in the grey shell (with thickness Δr) at Euclidean distance r from the target particle. Particles with different colour locate in the shell with different r. After normalising the r using d_m, the coloured particle can be represented by the corresponding shaded range of r/d_m. The right plot is a zoom-in illustration for the case $\eta = 1.1$ for $r/d_m \in [1.4, 2.4]$. Note that $g(r)$ of all cases tends to converge at 1 when r/d_m reaches 7
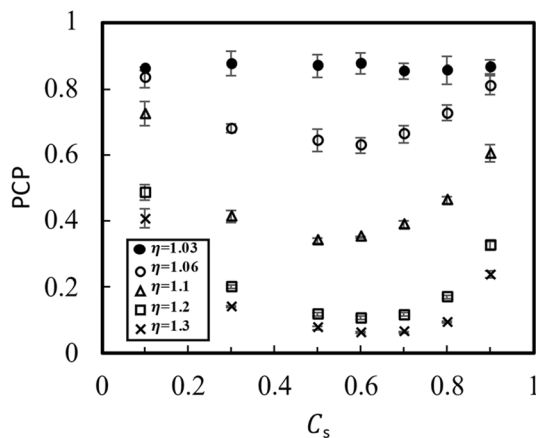

Fig. 7 Percentage of crystallised particles, PCP, vs the size ratio (η) and number fraction of small particles (C_s). Error bars, i.e. standard deviation, indicate that results of each point are based on five simulations

in Sect. 3.1, the centre of small particles can be slightly closer to the plate, which can result in larger and unnecessary overlaps between small and large particles when observing from out of the plane. This discrepancy may result in uncertainties for the final ϕ. However, the η is considerably small in the experiment described in Sect. 3.1; thus, the uncertainties can be negligible here.

The poly-disperse cases can be extended by adding particles with more varying sizes into the bi-disperse assemblies. To achieve this, a certain extent of particle size distribution, e.g. normal distribution, can be applied by controlling the mean size and standard deviation. When the sample size is limited, i.e. only three or five sizes to form the distribution, the size and content of each particle type can be crucial to the results [52].

The grain transformation of bi-disperse granular assemblies can be helpful to explain the desiccation crack within the extremely fine particle clusters, such as clay and starch, caused by the drying out of the moisture. In these materials, particles shape normally are uniform while the size may vary slightly to form a slight poly-disperse or bi-disperse assemblies, taking $\eta = 1.2$ in this study as an example. In this case, the polycrystalline structure can be formed which, to some extent, results in grain orientation diversity among grains, thus further influence the evaporation and mechanical property of the whole structure.

5 Conclusion

To investigate order and disorder morphological structures within bi-disperse particle assemblies in pseudo-2D condition, a series of DEM packing simulations have been conducted, alongside with a 2D packing experiments for validation purposes. Mono-disperse and poly-disperse circular discs have been simulated in previous studies, while the investigation here mainly focuses on the effect of size ratio, η, and the number fraction of small particles, C_s, in spherical particle samples.

Fig. 8 Heat map of the percentage of crystallised particles, PCP, alongside with six crystallised grain orientation plots. The grain orientation diversity is more obvious when varying the combination of η and C_s
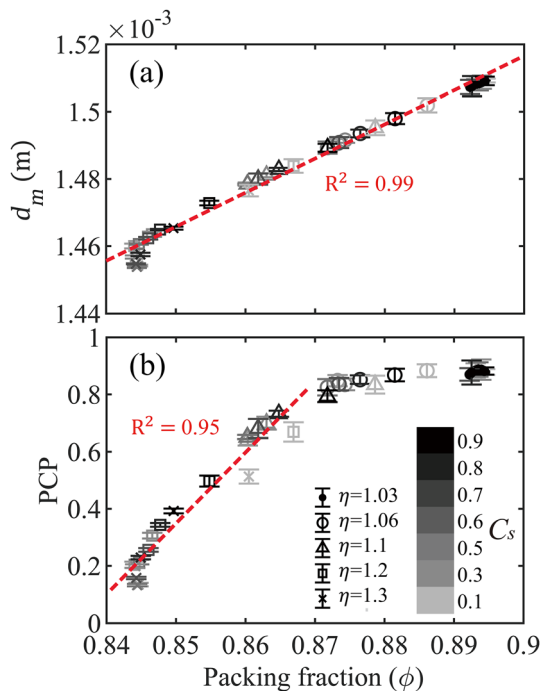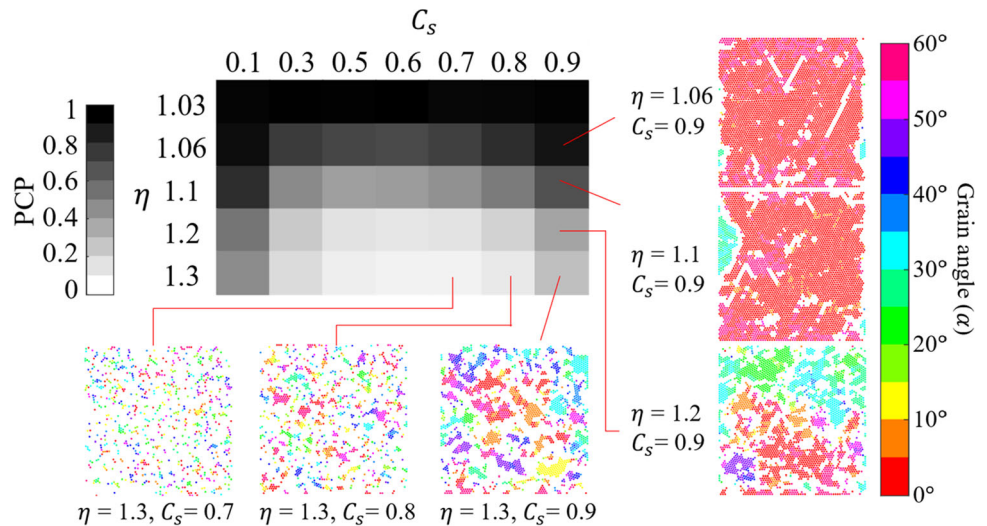

$\eta = 1.3, C_s = 0.7$ $\eta = 1.3, C_s = 0.8$ $\eta = 1.3, C_s = 0.9$

Fig. 9 Quantitative characterisation of all packing simulation cases: **a** Average diameters, d_m, of particles are linearly related to the ϕ. **b** The PCP can be a function of packing fraction ϕ with a linear-like trend until $\phi \approx 0.87$, which is larger than random close packing [13]. The marker symbolises the size ratio (η). The greyscale colour coding from light grey to black represents C_s ranges from 0.1 to 0.9

structure. During these processes mentioned above, it can be found that single crystalline structure can gradually transition to the polycrystalline structure until the crystallisation fully disappears. Some extent of diversity of grain orientation can raise due to the different combination of size ratio and bi-disperse number fraction.

The results can give clues on how the mixed binary number fraction can have effects on the morphological change for the granular sample. The 2D case may not be able to capture all the phenomenon, especially compared with the 3D case, but it can effectively evidence that how the mixed binary number fraction affects the packing fraction in 3D [21]. Further investigation on the roughness, shape of particles and larger size ratio may be worthwhile since the contact relation changed by those factors may also be dominant for the order and disorder state.

Firstly, the combined procedure of size growth and dynamic vibration is proved to be effective to reproduce a disorder to order transition within the mono-dispersed granular assemblies. The mixture of bi-dispersed particles with varying η and C_s can, to some extent, suppresses the crystallisation when η is raised from 1.06. Meanwhile, C_s converges from extreme values, e.g. 0.1 or 0.9, to the mid-range values are also crucial to impede the ordered

References

1. Vijayan, A., Gan, Y., Annabattula, R.K.: Evolution of fabric in spherical granular assemblies under the influence of various loading conditions through DEM. Granular Matter **22**(2), 34 (2020)
2. Farhadi, S., Zhu, A.Z., Behringer, R.P.: Stress relaxation for granular materials near jamming under cyclic compression. Phys. Rev. Lett. **115**(18), 188001 (2015)
3. Zhai, C., Herbold, E.B., Hurley, R.C.: The influence of packing structure and interparticle forces on ultrasound transmission in granular media. Proc. Natl. Acad. Sci. **117**, 16234–16242 (2020)
4. Gan, Y., et al.: A particle-water based model for water retention hysteresis. Géotech. Lett. **3**, 152–161 (2013)
5. Jarray, A., et al.: Cohesion-driven mixing and segregation of dry granular media. Scientific reports **9**(1), 1–12 (2019)
6. Dai, W., et al.: Influence of gas pressure on the effective thermal conductivity of ceramic breeder pebble beds. Fusion Eng. Des. **118**, 45–51 (2017)

7. Dai, W., Hanaor, D., Gan, Y.: The effects of packing structure on the effective thermal conductivity of granular media: a grain scale investigation. Int. J. Therm. Sci. **142**, 266–279 (2019)

8. Zhai, C., Gan, Y.: Electrical percolation in conductive granular media. J. Coupled Syst. Multisc. Dyn. **6**(4), 310–316 (2018)

9. Creyssels, M., et al.: Some aspects of electrical conduction in granular systems of various dimensions. Eur. Phys. J. E **23**(3), 255–264 (2007)

10. Sangrós Giménez, C., et al.: Mechanical, electrical, and ionic behavior of lithium-ion battery electrodes via discrete element method simulations. Energy Technol. **8**(2), 1900180 (2020)

11. Hwang, H., et al.: 2D percolation design with conductive microparticles for low-strain detection in a stretchable sensor. Adv. Funct. Mater. **30**(13), 1908514 (2020)

12. Majmudar, T., et al.: Jamming transition in granular systems. Phys. Rev. Lett. **98**(5), 058001 (2007)

13. Dong, K.J., et al.: Critical states and phase diagram in the packing of uniform spheres. EPL (Europhys. Lett.) **86**(4), 46003 (2009)

14. Sastry, S.: Critically jammed. Proc. Natl. Acad. Sci. **113**(35), 9673–9675 (2016)

15. An, X., et al.: Packing densification of binary mixtures of spheres and cubes subjected to 3D mechanical vibrations. Appl. Phys. A **118**(1), 151–162 (2015)

16. An, X., et al.: DEM study of crystallization of monosized spheres under mechanical vibrations. Comput. Phys. Commun. **182**(9), 1989–1994 (2011)

17. Yerazunis, S., Cornell, S., Wintner, B.: Dense random packing of binary mixtures of spheres. Nature **207**(4999), 835 (1965)

18. Amirifar, R., et al.: Self-assembly of granular spheres under one-dimensional vibration. Soft Matter **14**(48), 9856–9869 (2018)

19. Scott, G., Kilgour, D.: The density of random close packing of spheres. J. Phys. D Appl. Phys. **2**(6), 863 (1969)

20. Dai, W., et al.: Modes of wall induced granular crystallisation in vibrational packing. Granular Matter **21**(2), 26 (2019)

21. Reimann, J., et al.: X-ray tomography investigations of mono-sized sphere packing structures in cylindrical containers. Powder Technol. **318**, 471–483 (2017)

22. Reimann, J., et al.: 3d tomography analysis of the packing structure of spherical particles in slender prismatic containers. Int. J. Mater. Res. **111**(1), 65–77 (2020)

23. Donev, A., et al.: Jamming in hard sphere and disk packings. J. Appl. Phys. **95**(3), 989–999 (2004)

24. Dong, K., et al.: Role of interparticle forces in the formation of random loose packing. Phys. Rev. Lett. **96**(14), 145505 (2006)

25. Farr, R.S., Groot, R.D.: Close packing density of polydisperse hard spheres. J. Chem. Phys. **131**(24), 244104 (2009)

26. Song, C., Wang, P., Makse, H.A.: A phase diagram for jammed matter. Nature **453**(7195), 629–632 (2008)

27. Borkovec, M., De Paris, W., Peikert, R.: The fractal dimension of the Apollonian sphere packing. Fractals **2**(04), 521–526 (1994)

28. Royall, C.P., et al.: Controlling competition between crystallization and glass formation in binary colloids with an external field. J. Phys.: Condens. Matter **20**(40), 404225 (2008)

29. Bai, Q., Mazza, M.G.: Crystallization via shaking in a granular gas with van der Waals interactions. Phys. Rev. E **100**(4), 042910 (2019)

30. Williams, S.R., Royall, C.P., Bryant, G.: Crystallization of dense binary hard-sphere mixtures with marginal size ratio. Phys. Rev. Lett. **100**(22), 225502 (2008)

31. Gan, Y., Rognon, P., Einav, I.: Phase transitions and cyclic pseudotachylyte formation in simulated faults. Philos. Mag. **92**(28–30), 3405–3417 (2012)

32. Sweijen, T., et al.: The effect of particle shape on porosity of swelling granular materials: discrete element method and the multi-sphere approximation. Powder Technol. **360**, 1295–1304 (2020)

33. Darde, B., et al.: Effects of the initial granular structure of clay sealing materials on their swelling properties: experiments and DEM simulations. EPJ Nuclear Sciences and Technologies **6**, 1 (2020)

34. Cheng, X.: Packing structure of a two-dimensional granular system through the jamming transition. Soft Matter **6**(13), 2931–2934 (2010)

35. MiDi, G.D.R.: On dense granular flows. Eur. Phys. J. E **14**(4), 341–365 (2004)

36. Rathbun, A.P., Marone, C.: Effect of strain localization on frictional behavior of sheared granular materials. J. Geophys. Res. Solid Earth (2010). https://doi.org/10.1029/2009JB006466

37. Fu, P., Dafalias, Y.F.: Quantification of large and localized deformation in granular materials. Int. J. Solids Struct. **49**(13), 1741–1752 (2012)

38. Gan, Y., Kamlah, M.: Discrete element modelling of pebble beds: with application to uniaxial compression tests of ceramic breeder pebble beds. J. Mech. Phys. Solids **58**(2), 129–144 (2010)

39. Rivas, N., et al.: Segregation in quasi-two-dimensional granular systems. New J. Phys. **13**(5), 055018 (2011)

40. Cundall, P.A., Strack, O.D.L.: A discrete numerical model for granular assemblies. Géotechnique **29**(1), 47–65 (1979)

41. Walton, O.R.: Numerical simulation of inclined chute flows of monodisperse, inelastic, frictional spheres. Mech. Mater. **16**(1–2), 239–247 (1993)

42. Luding, S.: Cohesive, frictional powders: contact models for tension. Granular Matter **10**(4), 235 (2008)

43. Kloss, C., et al.: Models, algorithms and validation for open-source DEM and CFD–DEM. Prog. Comput. Fluid Dyn. Int. J. **12**(2–3), 140–152 (2012)

44. Singh, A., et al.: The role of gravity or pressure and contact stiffness in granular rheology. New J. Phys. **17**(4), 043028 (2015)

45. Komatsu, Y., Tanaka, H.: Roles of energy dissipation in a liquid-solid transition of out-of-equilibrium systems. Phys. Rev. X **5**(3), 031025 (2015)

46. Ganapathi, D., et al.: Structure determines where crystallization occurs in a soft colloidal glass. Nat. Phys. **17**, 114–120 (2020)

47. Desu, R.K., Moorthy, A., Annabattula, R.K.: DEM simulation of packing mono-sized pebbles into prismatic containers through different filling strategies. Fusion Eng. Des. **127**, 259–266 (2018)

48. Rietz, F., et al.: Nucleation in sheared granular matter. Phys. Rev. Lett. **120**(5), 055701 (2018)

49. Daniels, K.E., Behringer, R.P.: Hysteresis and competition between disorder and crystallization in sheared and vibrated granular flow. Phys. Rev. Lett. **94**(16), 168001 (2005)

50. Jung, G., Petersen, C.F.: Confinement-induced demixing and crystallization. Phys. Rev. Res. **2**(3), 033207 (2020)

51. Meng, L., Lu, P., Li, S.: Packing properties of binary mixtures in disordered sphere systems. Particuology **16**, 155–166 (2014)

52. Desu, R.K., Annabattula, R.K.: Particle size effects on the contact force distribution in compacted polydisperse granular assemblies. Granular Matter **21**(2), 29 (2019)